Study of Microporosity Formation under Different Pouring Conditions in A356 Aluminum Alloy Castings

Lu Yao, Steve Cockcroft, Daan Maijer, Jindong Zhu and Carl Reilly

Department of materials engineering, University of British Columbia, 309-6350 Stores Road, Vancouver, B.C.
Canada V6T 1Z4

Abstract

In this work, the formation of microporosity has been examined under different casting conditions aimed at manipulating the tendency to form and entrain oxide films in small directionally cast A356 samples. Porous disc filtration analysis (PoDFA) was used to assess the melt cleanliness and identify the inclusions in the castings. The porosity volume fraction and size distribution were measured using X-ray micro-tomography (XMT) analysis. By fitting a pore formation model to the experimental results, an estimate of the pore nucleation population has been made. The results from the model predictions indicate that increasing the tendency to form and entrain oxide films not only increases the number of nucleation sites but also reduces the supersaturation necessary for pore nucleation in A356 castings.

Introduction

The limited understanding of the nucleation mechanism is one of the main challenges still to be overcome in simulating microporosity formation in aluminum alloy castings. Previous studies have shown that porosity formation can be significantly influenced by inclusions, especially oxide films in the melt [1-6]. Conventional theories suggest that solid inclusions in the melt provide heterogeneous nucleation sites, which reduce the nucleation energy barrier required for pore nucleation [3, 7, 8]. In this theory, pore nucleation is promoted by a smaller contact angle between the liquid/pore interface and the solid substrate. This theory has been questioned by Campbell, who pointed out heterogeneous nucleation seems highly improbable due to the restriction on the minimum contact angle attainable, which is observed as close to 20 degrees in practice [9]. He proposed a nucleation-free mechanism for porosity formation based on a continuous solid oxide film present on the free surface of the liquid in aluminum alloys [9-11]. Due to free-surface turbulence (such as occurs during pouring), the oxide film becomes entrained in the melt and are often broken and folded as double-sided films. Within these oxide films it is proposed that air is entrapped and becomes a gas cavity. These gas cavities can be considered as preexisting pores in the melt. Pore growth can occur by hydrogen diffusion to these gas cavities and/or the unfurling of the bi-films due to a drop in the surrounding pressure associated with high fraction solid restricted feeding. This theory has gained considerable attention in the field of aluminum alloy casting research; however, no direct experimental evidence has been provided because of the nanometer scale thickness and transparent nature of the bi-films. The identification of the pore/oxide film interaction mechanism is still a subject of active research.

The main objective of this work is to study the effect of oxide film content on microporosity formation in A356 aluminum alloy castings. The focus is on oxide films formed during the pouring process, as studies have shown that pouring generates the largest free surface area during a gravity casting process [12]. The approach involves estimating the pore nucleation population by fitting a pore size distribution, which is predicted by a comprehensive mathematical model, to data obtained from a series of experimental castings in which the pouring conditions were varied. The results are discussed in terms of nucleation number density and nucleation potency (the latter defined as the supersaturation necessary for pore nucleation). In addition to the role of oxide film inclusions, the effect of hydrogen content and Sr modification on microporosity nucleation is also discussed.

Experimental method

Casting procedures

A series of experimental castings of A356 alloy were directionally solidified in a tapered, cylindrical refractory ceramic mold against a water-cooled copper chill under different pouring conditions conducive to varying the entrained oxide film content. To quantify the cooling conditions within the casting the evolution of temperature with time was measured with three K-type thermocouples positioned within the mold cavity at 10, 30 and 50 mm from the chill, as shown in Figure 1. To determine the hydrogen content, Ransley samples were cast, machined and analyzed using the LECO vacuum fusion technique, which is accurate to within 0.01 ppm. In order to vary the tendency to form and entrain oxide films within the casting, three different pouring methods were adopted: 1) normal pouring (intermediate tendency), Figure 1 (a); 2) Ar-shielded pouring (low tendency), Figure 1 (b); and 3) high-surface area pouring (high tendency), Figure 1 (c). In the first and second methods, the pour surface area was held constant, but shielding with argon in the second method decreased the ambient oxygen content. In the third method, the pour surface area was increased relative to the base or
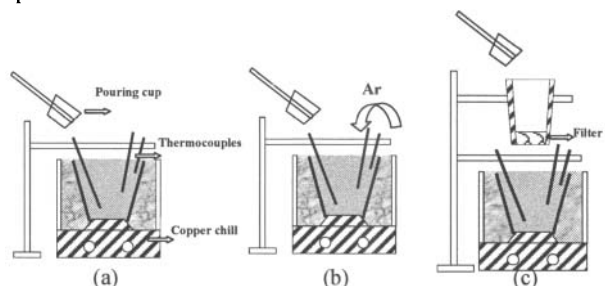

Figure 1. Schematic of the experiment setup for (a) normal pouring (NP), (b) Ar shielded pouring (ArP) and (c) high surface area pouring (HSAP) conditions.

Table I. Summary of pouring conditions

Sample Label / Casting Condition	CAPTN-NP	CAPTIN-NPL	CAPTIN-ArP	UBC-NP	UBC-HSAP
Metal Source	Alcoa	Alcoa	Alcoa	Rio Tinto Alcan	Rio Tinto Alcan
Ar Shielding	No	No	Yes	No	No
Pouring Surface Area	Normal	Normal	Normal	Normal	High
Hydrogen Content (ppm)	0.30±0.01	0.17±0.01	0.35±0.01	0.28±0.01	0.30±0.01

Table II. Chemical composition analysis for A356 aluminum alloy samples cast at CAPTIN and UBC (weight percentage)

	Si	Mg	Fe	Ti	Sr	Al
CAPTIN	6.89	0.34	0.15	0.13	0.0092	Bal.
UBC	7.49	0.38	0.10	0.10	0.0030	Bal.

normal case by pouring the metal into a course 20 ppi reticulated foam filter installed above the mould (unsaturated filtration). The filter acted to separate the liquid metal into several pour streams thereby increasing the surface area in contact with ambient air.

Effect of Ar shielding. This component of the experimental work was undertaken at Canadian Auto Parts Toyota Inc. (CAPTIN) at their wheel casting facility located in Delta, BC, Canada. The A356 alloy was comprised of ingot from Alcoa and some revert from the plant. The metal was melted in a commercial reverberatory furnace, poured into a ladle and Sr was added for modification. The metal was not degassed. A boron-nitride coated, steel, pouring cup was used to transfer the metal from the ladle and pour it into the mould. The melt temperature was ~710 °C at the time it was poured.

In addition to assessing the effect of Ar shielding at CAPTIN, there was one additional test completed with no Ar shielding in which the metal contained a lower hydrogen concentration. This difference arose due to differences in ambient humidity or holding time in the melt furnace, not degassing.

Effect of Pour Surface Area. The second casting campaign was undertaken in the Advanced Materials and Process Engineering Laboratory (AMPEL) at University of British Columbia. Ingots sourced from Rio Tinto Alcan were melted in a graphite crucible using a lab-scale resistance furnace and held at 800°C for approximately 3hrs. In preparation for casting, 0.5 g of Al-15 wt% Sr alloy was added, the melt was held for a further 10 minutes for homogenization and the surface was skimmed to remove the accumulated dross. The melt was then finally poured at ~750 °C. A higher pouring temperature was used to increase fluidity of the melt and enable it to pass through the filter.

The casting conditions and labels assigned to each of the cases for the purpose of discussion are summarized in Table I. The chemical compositions of the cast samples from the two sets of experiments are shown in Table II.

Inclusion analysis

Concurrent with the casting operation, porous disc filtration analysis (PoDFA) samples were taken under each casting condition to measure the type and content of inclusions. The PoDFA was undertaken following the instructions [14] established by BOMEM Inc., Quebec, Canada. The procedure entailed pouring 1 kg of melt into a crucible where it was forced to flow through a fine filter under pressure. During filtration,

concentrated impurities and particulates from the melt are accumulated above the filter in the so-called 'cake'. The PoDFA sample included the residual metal, the inclusion cake and the filter, which was analyzed using standard metallographic procedures by Rio Tinto Alcan Limited, Arvida Research and Development Centre (ARDC), Jonquiere, Quebec, Canada. The types of inclusions present were identified under an optical microscope by comparison with documented images of the inclusions based on their morphological and chemical characteristics. The total area of each type of inclusions was measured using the grid method and divided by the total mass of the filtered melt to calculate the inclusion content. The results were given in the unit of mm^2/kg.

X-ray micro-tomography (XMT) analysis

The cast porosity volume fraction and size distribution were measured using 3D X-ray micro-tomography (XMT). A 3mm diameter cylinder of material was machined from the centre of each casting. Three scans were performed on each cylinder at 10, 30 and 50mm from the chill, corresponding to where the thermocouples were positioned. Each scan was comprised of 500 slices with a diameter of 3 mm and a volume of 13.1 mm^3. The three-dimensional images of the pores were generated from these 500 slices (2-D X-ray images) using the software ImageJ and AMIRA. The scans were conducted using the synchrotron X-ray microscope located in the TOMCAT lab at the Swiss Light Source (SLS), Paul Scherrer-Institute, Villigen, Switzerland. The tomography data were acquired by applying a beam energy of 27 keV and a resolution of 3.7 μm.

Numerical model

The readers are referred to reference [15] for details of the pore nucleation and growth model developed previously to predict the microporosity formation in A356 castings. Here only some key concepts in the model are presented for the sake of brevity.

The model accounts for pore nucleation assuming a relationship between nucleation site distribution and the supersaturation of the liquid. The nucleation site distribution is defined as the change of the number of nucleation sites due to hydrogen supersaturation. The numerical form of the microporosity nucleation site distribution is a Gaussian function of hydrogen supersaturation, ss, as presented in Equation (1):

$$\frac{dN_{nuc}}{dss} = \frac{A}{\sqrt{2\pi}\sigma}\exp(-\frac{(ss-ss_0)^2}{2\sigma^2})$$ (1)

Table III. Results from PoDFA analysis showing major inclusions found in samples cast at CAPTIN and UBC

Sample Inclusion Type	CAPTIN-NP (mm^2/kg)	CAPTIN-NPL (mm^2/kg)	CAPTIN-ArP (mm^2/kg)	UBC-NP (mm^2/kg)	UBC-HSAP (mm^2/kg)
Al_4C_3($\leq 3\mu m$)	0.47	0.18	0.49	0.26	0.03
Al_4C_3($\geq 3\mu m$)	0.86	0.72	0.49	-	-
$MgAl_2O_4$	-	-	-	0.22	Trace
(TiV)B_2	-	-	-	0.06	Trace
TiB_2/TiC	-	-	-	1.46	0.79

where A, ss_0 and σ are parameters describing pore nucleation kinetics. ss_0 (mol/m^3) is the mean hydrogen super-saturation required for pore nucleation, which may be equated with the potency of the pore nucleation population in the melt. σ (mol/m^3) is the width of the nucleation site distribution, which may be equated with the variability in potency of the population. In this work, A is determined by the number of pores near the chill bottom measured from XMT experimental data. This assumes that the supersaturation achieved near the chill exceeds $ss_0 + 3\sigma$ – i.e. full integration of Equation (1) gives A. The highest supersaturations are achieved at the chill because of the high cooling rates present there.

Pore growth is simulated as a hydrogen diffusion controlled process. The mass transfer rate of hydrogen is evaluated according to Equation (2).

$$\frac{dm_H}{dt} = D_l \cdot 4\pi r_p^2 \cdot \phi \cdot (C_l - C_{lp})/l_{diff} \qquad (2)$$

where m_H (mol) is the number of moles of hydrogen transported to the pore, D_l (m^2/s) is diffusivity of hydrogen in the liquid A356 alloy, r_p(m) is the radius of the growing pore, l_{diff} (m) is the thickness of the diffusion boundary layer, approximated as the pore radius, and ϕ is factor used to account for the reduction in pore surface area in contact with liquid metal as the solid fraction increases during solidification. The impingement factor is assumed to be equal to $(1-f_s)^m$, where f_s is the solid fraction and m is a parameter to be determined by fitting with experimental data.

Experimental results

Inclusion analysis based on PoDFA measurement

Originally, the PoDFA inclusion analysis was undertaken in an attempt to quantify the oxide film content in the melt. Table III shows the types and quantity (expressed in units of specific area) of the main inclusions identified in the analysis for both the Alcoa and Rio Tinto Alcan alloys under different pouring conditions at CAPTIN and UBC. In addition to the inclusions shown in Table III, traces of chlorides, MgO, graphite and refractory materials were also observed.

There are a couple of observations that can be made from the results of the PoDFA analysis. Firstly, quantification of oxide film content proved to be difficult as only a limited number of the oxide films were detected. Secondly, based on the inclusions that could be identified, the coarse filter used to produce the UBC-HSAP sample was able to "clean the melt", as evidenced by a reduction in the surface area of inclusions in the filter residue.

To follow up on the lack of oxide films observed in the PoDFA[TM1]

---
[1] PoDFA is a trademark of Rio Tinto Alcan Inc.

analysis, an analysis of the filter cake was undertaken using an SEM. The SEM analysis was able to identify structures that appeared to be film like. Furthermore and more relevant, EDX mapping of pores found in the PoDFA filter residue using the SEM have showed the presence of oxygen associated with pores. An example image is shown in Figure 2. This observation appears consistent with microporosity nucleation on oxide film inclusions. Unfortunately, it proved impossible to quantify the area fraction or number of oxide films present in the various samples of filter cake using the SEM.
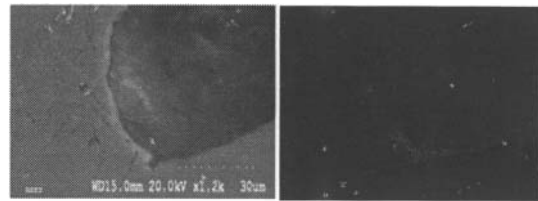

Figure 2. EDX mapping analysis that shows presence of oxygen associated with pores.

Microporosity analysis from XMT measurement

The XMT data from the samples cast under the different conditions was analyzed and the volume fraction, number density and size distribution of the pores as a function of distance from the chill was determined. The data is presented as: 1) plots of volume fraction and number density vs. distance from the chill – see Figures 3, 5 and 7; 2) a 2D projection of the 3D rendering of pores at 10, 30 and 50mm from the chill – see Figures 4, 6 and 8; and 3) a size distribution plot (number density vs. pore radius) – see Figures 4, 6 and 8. In the line graphs, the experimental results appear as the symbols, where as in the size distribution plot (bar chart) the experimental data appears as the shaded bars. The error bars for volume fraction indicate the potential deviation in the measurement related to choice of gray scale threshold used to distinguish the pores from matrix in the XMT analysis [15].

Effect of hydrogen content and Cooling Rate. The effect of hydrogen content on porosity is shown in Figures 3 and 4, in which the CAPTIN-NP and CAPTIN-NPL samples are compared. The CAPTIN-NP sample contained 0.30±0.01 ppm hydrogen and the CAPTIN-NPL sample contained 0.17±0.01 ppm hydrogen. As expected the higher hydrogen content yields a higher volume fraction of pores, which is a consequence of the higher pore number density in Figure 3(a) and trend to larger pore sizes in Figure 4. The high degree of sensitivity to hydrogen content is well established [4,5]. In addition, the data also shows a strong dependence on cooling rate with the trend to fewer (Figure 3(a)) larger pores (Figure 4) with increasing distance from the chill. The trend to fewer pores with increasing distance from the chill

785

(decreasing cooling rate) relates to the nucleation process and points to the fact that there is some mechanism by which the number of nuclei activated is sensitive to cooling rate. The mechanism is discussed in more detail with the aid of the numerical analysis.
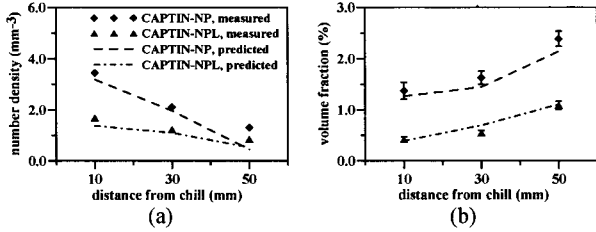
would have normally resulted in an increase volume fraction and trend to larger pores as previously discussed.

Figure 3.Comparison between measured (symbol) and predicted (dashed line) pore volume fraction and number density in samples resulted from medium and high hydrogen levels.
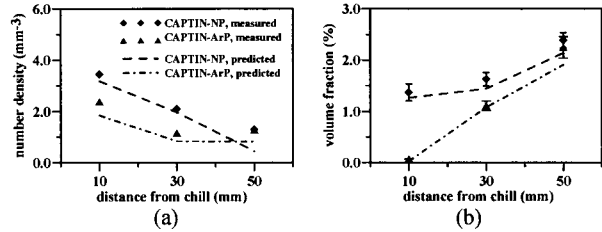

Figure 5.Comparison between measured (symbol) and predicted (dashed line) pore volume fraction and number density in samples resulted from normal pouring (CAPTIN-NP) and Ar shielded pouring (CAPTIN-ArP) conditions.
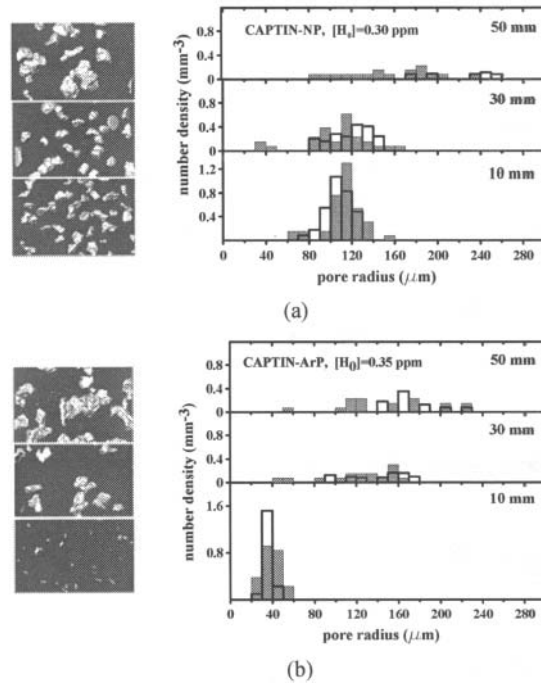

Figure 4.Comparison between measured (solid columns) and predicted (transparent columns) pore size distribution at different distances from the chill in samples resulted from (a) medium and (b) high hydrogen levels.

Figure 6.Comparison between measured(gray columns) and predicted(transparent columns) pore size distribution at different distances from the chill in samples resulted from (a) normal pouring (CAPTIN-NP) and (b)Ar shielded pouring (CAPTIN-ArP) conditions.

Effect of Ar shielded pouring. Figures 5 and 6 compare the volume fraction and pore size distributions resulting from the normal and Ar shielded pouring (CAPTIN-NP and CAPTIN-ArP). From the various plots it is clear that the volume fraction, pore number and pore size all decrease under Ar shielded pouring. As there is higher hydrogen content in the CAPTIN-ArP sample (0.35 ±0.01 ppm) compared with the CAPTIN-NP sample (0.30±0.01ppm), the decreased in volume fraction and tendency to smaller pore sizes under Ar shielded pouring must relate to difference in the nucleation population – i.e. a shift to higher supersaturations and higher fraction solid. In the absence of a change in the nucleation processes, the higher hydrogen content

Effect of high-surface area pouring. The results from XMT measurement of the pore volume fraction, number density and size distribution under normal and high-surface area pouring conditions are shown in Figure 7 and 8. The results indicate a significant increase in the volume fraction and pore size in the high surface area casting (UBC-HSAP) relative to the normal pouring condition (UBC-NP). Interestingly, there is no significant difference in the number density of pores. It is also important to point out that the UBC-HSAP casting contained slightly more hydrogen than the UBC-NP casting (0.30 vs 0.28ppm) and thus it is difficult to conclude that the difference observed is due to a difference in nucleation population resulting from a change in tendency to form oxide films or is due to the difference in

hydrogen content. The final conclusion will need to be deferred until the model-based analysis of the data has been completed.
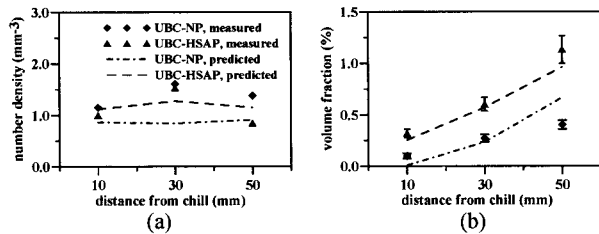

Figure 7.comparison between measured (symbol) and predicted (dashed line) pore volume fraction and number density in samples resulted from normal pouring (UBC-NP) and high-surface-area pouring (UBC-HSAP) conditions.
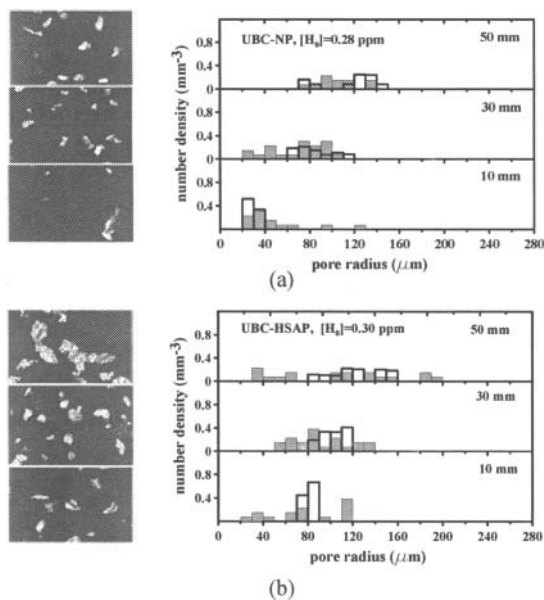

Figure 8.Comparison between measured (gray columns) and predicted (transparent columns) pore size distribution at different distances from the chill in samples resulted from (a) normal pouring (UBC-NP) and (b) high-surface-area pouring (UBC-NSAP) conditions.

Mathematical Model Analysis

To help better understand the role of oxidation tendency on nucleation kinetics, the castings have been analyzed using a comprehensive pore nucleation and growth model. The only 'fitting parameters' used in the model are those related to the description of the pore nucleation kinetics and pore/solid impingement; namely ss_0, σ and m.

A trial and error approach was applied for each casting to determine the fitting parameters that gave the best fit for the entire casting. Comparisons between the model predictions and XMT measurements can be found in Figures 3 through 8. In the line graphs, Figures 3, 5 and 7, the model predictions appear as the lines. In the distribution plots (bar charts) the model predictions appear as the un-shaded bars. As can be seen, the model is able to

accurately reproduce the variation in volume fraction and number density of pores with distance from the chill quantitatively at most of the comparison points. Furthermore, the model is also able to reproduce the pore size distribution observed in the sample to within a reasonable degree of accuracy.

Beginning first with the impingement factor, as the impingement factor is linked to the solidification morphology, it should only be dependent on cooling rate and alloy composition, not the pouring condition. Figure 9 shows the impingement factor m as a function of cooling rate determined by fitting with the experimental measurements. The variation of m with cooling rate is consistent with a reduction in impingement with decreasing cooling rate (increasing grain size). It can also be seen that a smaller m was applied for the CAPTIN samples, corresponding to a lower impingement between pores and solid grains at a given fraction solid. This can be explained by comparing the microstructures of the CAPTIN and UBC metal, shown in Figure 10. As can seen the CAPTIN metal (Figure 10 (a)) solidifies into a structure that is more globular dendritic than the UBC material. As a result, one would expect a smaller pore/solid impingement in the CAPTIN structure at a given solid fraction. Within a given alloy group – i.e. CAPTIN vs UBC metal – it was possible to use a single cooling rate dependent m, for evaluation of the various pouring conditions.
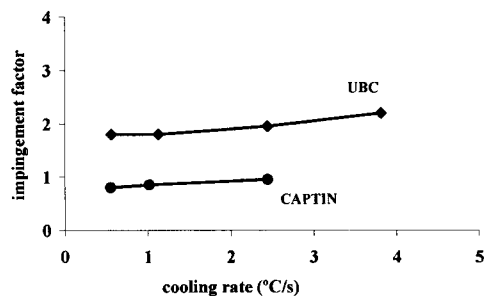

Figure 9.Impingement factor m as a function of distance from the chill derived by fitting the model predictions with experimental measurement.

Figure 11 shows the model-predicted nucleation site distributions that yielded the best fit to the measured porosity data for the different pouring conditions. Note the same nucleation distribution was used for both the CAPTIN-NP and CAPTIN NPL samples (consistent with the fact that the same pouring procedure was used for both). The results for the different pouring scenarios
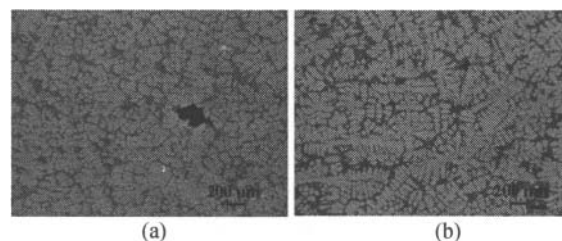

Figure 10.Optical micrograph of as-cast microstructures in samples resulted from different metal sources at (a) CAPTIN and (b) UBC.

indicate both a difference in the potency of the nucleation population, as indicated by a difference in ss_0, and a difference in the number of available nucleation sites, as indicated by differences in A dependent on the casting conditions - refer to Equation (1).

The effect of cooling rate on pour nucleation can be understood by considering the variation in supersaturation with cooling rate. Analysis with the model has revealed that the highest supersaturations are reached near the chill, hence the largest number of nuclei become activated at the chill. As previously described, this behavior was used to reduce the number of fitting parameters in the model – i.e. the value of A was determined from the pore number density measured at the chill (10mm location). This approach appears to have achieved good results overall, but it should be pointed out that it will work only if the initial hydrogen content is sufficiently high. For example, in the case of the CAPTIN-NPL sample, the analysis with the model revealed that at the lower initial hydrogen content of 0.17ppm, not all of the pores were activated at the chill, hence it was possible to achieve a good fit consistent with the measurements with a single nucleation population.

The effect of Ar shielding on the nucleation site distribution can be seen by comparing the results for samples CAPTIN-NP and CAPTIN-ArP in Figure 11. The nucleation potency is reduced when Ar shielding is applied, as indicated by an increase of ss_0 from 2.5 mol/m³ to 8.5 mol/m³. The total number of nucleation sites is also reduced for the Ar shielded pouring condition, indicated by a decrease of A from 3.5 per mm³ to 2.5 per mm³. The change is consistent with Ar shielding reducing the tendency to form and entrain oxide films.

The effect of pour surface area is shown by comparing the nucleation curves for samples UBC-NP and UBC-HSAP in Figure 11. The nucleation potency is increased when the melt is poured with an increased surface area as indicated by a decrease of ss_0 from 0.40 mol/m³ to 0.25 mol/m³. In addition there is also an increase in the total number of nucleation sites from 1.1 per mm³ to 1.5 per mm³. This result is obtained despite a decrease in the Al_4C_3, $MgAl_2O_4$, $(TiV)B_2$ and TiB_2/TiC content as shown in Table III. This is consistent with literature were it has been argued previously that carbides are not effective as nucleation sites for hydrogen porosity [9].
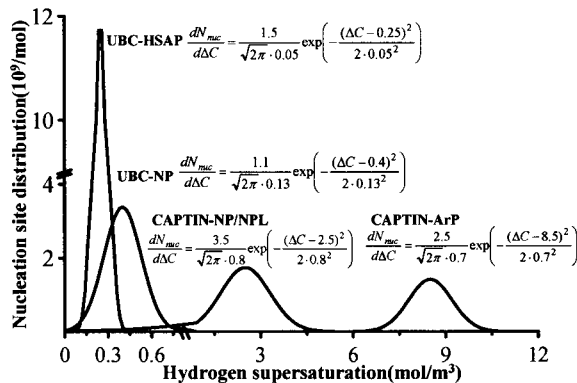

Figure 11.Pore nucleation site distribution under various casting conditions derived by fitting the model predictions with experimental measurements.

Another observation that can be made from Figure 11 is that there is a clear difference between the nucleation population present in the samples cast at UBC and those cast at CAPTIN. The exact reason for this difference is unclear. Based on the PoDFA analysis the UBC metal is the cleaner of the two, which is consistent with the fact that it was produced from virgin ingot (the CAPTIN material contained some revert). A closer look at the difference in metal composition (see Table II) reveals a significant difference in the Sr levels - 0.0092 for CAPTIN material and 0.0030 for the UBC material. Work is currently underway, including a review of the literature, to better understand what potential role Sr, a strong surface tension modifier, will have on nucleation of hydrogen.

Summary and Conclusions

The effect of varying the tendency to form and entrain oxide films on microporosity nucleation kinetics has been investigated in this work by altering the method in which small directional solidified castings were poured. Changes to the pouring method entailed Ar shielding and increasing the pour stream surface area relative to a base case. The effect of these changes was quantified by measuring the porosity volume fraction, pore number density and pore size distribution as a function of distance from the chill via 3D XMT analysis. By fitting the predictions of a comprehensive pore numerical model to the XMT measurements, differences in the nucleation kinetics have been estimated for the different pouring conditions. The methodology involved adjusting the parameters used to define the nucleation behavior, by trial and error, until good agreement was obtained with the results of the experiments. The results tend to support the hypotheses that oxide films provide good nucleation sites for pore formation in-so-far as increasing and decreasing the tendency to form and entrain oxides in association with the pouring process resulted in a consistent increase and decrease, respectively, in the porosity volume fraction. It was also observed that changes in pour stream oxidation tendency result in both changes in the number of pore nucleation sites and potency (supersaturation) of the sites. The results do not support or refute the bi-film mechanism proposed by Campbell [9-11]. They simply confirm that altering the tendency to form and entrain oxide films alters the tendency to form pores in a manner consistent with oxide films playing a role in the nucleation of hydrogen based pores.

Acknowledgment

References

1. D. Emadi, J. E. Gruzleski and M. Pekguleryuz, "Melt Oxidation Behavior and Inclusion Content in Unmodified and Sr-Modified A356 Alloy-Their Role in Pore Nucleation", AFS Transactions, 104 (1996), 763–768.
2. G. Laslaz and P. Laty, "Gas Porosity and Metal Cleanliness in Aluminum Casting Alloys", AFS Transactions, 99(1991), 83-90.
3. X. G. Chen and S. Engler, "Formation of Gas Porosity in Aluminum Alloys", AFS Transactions, 102(1994), 673-682.
4. K. Tynelius, J. F. Major and D. Apelian, "A Parametric Study of Microporosity in the A356 Casting Alloy System", AFS Transactions, 101(1993), 401-413.

5. D. Emadi and J. E. Gruzleski, "Effect of Castings and Melt Variables on Porosity in Directionally-Solidified Al-Si Alloys", *AFS Transactions*, 102(1994), 307-312.

6. L. Liu,A. M. Samuel and F. H. Samuel, "Influence of Oxides on Porosity Formation in Sr-treated Al-Si casting alloys", *Journal of Materials Science*, 38(2003),1255-1267.

7. M. Massoud, *Engineering Thermofluids: Thermodynamics, Fluid Mechanics, and Heat Transfer*, (Springer Berlin Heidelberg, 2005),637-641.

8. S. F. Johes, G. M. Evans and K. P. Galvin, "Bubble Nucleation from Gas Cavities: a Review", *Advances in Colloid and Interface Science*, 80(1999), 27-50.

9. J. Campbell, *Castings*. (Butterworth Heinemann, 2 ed., 2003), 179-181.

10. D. Dispinar and J. Campbell, "Critical Assessment of Reduced Pressure Test. Part 1: Porosity Phenomena", *International Journal of Cast Metals Research*, 17(5) (2004), 280-286.

11. J. Campbell, "Entrainment Defects", *Materials Science and Technology*, 22(2) (2006), 127-145.

12. N. W. Lai, W. D. Griffiths and J. Campbell, "Modelling of the Potential for Oxide Film Entrainment in Light Metal Alloy Castings", *Modeling of Casting, Welding and Advanced Solidification Process*, (2003), 415-422.

13. O. Lashkari et al., "X-Ray Microtomographic Characterization of Porosity in Aluminum Alloy A356", *Metallurgical and Materials Transaction*, 40A (2009), 991-999.

14. PoDFA-f user's Manual, Revision 1-0, March 1999. ABB Bomen Inc.

15. L. Yao et al., "Modeling of Porosity Size Distribution in A356 Tapered Cylinder Castings", *Modeling of Casting, Welding and Advanced Solidification Process*, (2009), 385-392.